2888 Vol. 13, No. 10 / October 2025 / *Photonics Research* **Research Article**

PHOTONICS Research

Chromatic optical coherence tomography for high-resolution deep tissue imaging

SEUNG EON LEE,[1] HYEONG SOO NAM,[1] RYEONG HYEON KIM,[2] HYUN JUNG KIM,[2] JAE YEON SEOK,[3] JIN WON KIM,[2] YOUNG-JIN KIM,[1] AND HONGKI YOO[1,*]

[1]*Department of Mechanical Engineering, Korea Advanced Institute of Science and Technology, Daejeon 34141, Republic of Korea*
[2]*Cardiovascular Center, Korea University Guro Hospital, Seoul 08308, Republic of Korea*
[3]*Department of Pathology, Yongin Severance Hospital, Yonsei University College of Medicine, Gyeonggi-do 16995, Republic of Korea*
**Corresponding author: h.yoo@kaist.ac.kr*

Received 7 March 2025; revised 9 July 2025; accepted 10 July 2025; posted 16 July 2025 (Doc. ID 561513); published 1 October 2025

Achieving clear and deep tissue imaging with optical coherence tomography (OCT) necessitates the simultaneous optimization of three critical factors: high resolution, extended depth of focus (DOF), and high signal-to-noise ratio (SNR). Conventional OCT systems often compromise one or more of these factors, due to inherent trade-offs in optical design and noise management. To address these limitations, we present a chromatic OCT system that simultaneously optimizes all three parameters. The system achieves an isotropic spatial resolution of 2 to 3 μm by leveraging a broad bandwidth light source and high-numerical-aperture optics with a pronounced chromatic focal shift, which enables up to a sevenfold DOF extension. Additionally, a novel noise-gating algorithm suppresses system-inherent noise, sidelobe artifacts, and multiple scattering effects, significantly enhancing the SNR. Comparative simulations and experiments demonstrate that the proposed chromatic OCT outperforms conventional high-resolution systems by maintaining superior resolution and SNR over an extended imaging range. These advancements establish chromatic OCT as a powerful tool for high-resolution, deep tissue imaging in biomedical applications, offering improved diagnostic capabilities.

https://doi.org/10.1364/PRJ.561513

1. INTRODUCTION

Optical coherence tomography (OCT) [1] is a widely utilized imaging modality renowned for its ability to deliver high-sensitivity cross-sectional images of human tissues. It plays a crucial role in detecting, diagnosing, and monitoring diseases across various biomedical fields [2–6]. However, the typical resolution of conventional OCT systems, ranging from 10 to 20 μm, limits their use as diagnostic tools for identifying pathobiological distinctions at the subcellular level. This limitation has led to considerable efforts to improve the OCT resolution down to the micrometer scale [7–11]. Enhancing the axial resolution is relatively straightforward and is achieved by using broadband light sources and detectors, leveraging the principle of coherent detection. On the other hand, enhancing the lateral resolution requires the use of high-numerical-aperture (NA) imaging optics, leading to a fundamental trade-off between the lateral resolution and depth of focus (DOF); reducing the beam size to a few micrometers drastically decreases the DOF to well below 100 μm, thereby significantly limiting the axial imaging range. Consequently, most high-resolution OCT systems tend to exhibit better axial than lateral resolutions [7,11–13].

While numerous efforts have been made to extend the axial imaging range of high-resolution OCT systems, a universally accepted solution remains elusive due to intrinsic trade-offs in each method. Some studies have attempted to address these trade-offs by computationally solving the inverse scattering problem [14,15], but these techniques require high phase stability among B-scan images, which limits their applicability, especially for dynamic *in vivo* imaging. Another common strategy involves transforming the Gaussian beam into a Bessel (or quasi-Bessel) beam using techniques such as apodization [11,16,17], binary phase filters [13,18–20], axicon lenses [21–23], and coaxially focused multimode beams [12,24,25]. However, these approaches are hindered by a decrease in signal-to-noise ratio (SNR) that is inversely proportional to the square of the DOF gain [26]. Moreover, the use of a Bessel beam introduces sidelobe artifacts, which further degrade the image quality and compromise the overall SNR. While the extended DOF of Bessel beam is beneficial for applications such as endoscopic OCT, where the distance between the imaging optics and sample surfaces varies, their reduced SNR still limits their use in deep tissue imaging.

Additionally, some researchers have explored the use of chromatic focal shifts in high-resolution OCT systems [27,28]. However, these studies rely on conventional Fourier transform (FT)-based image reconstruction algorithms, which are not optimized for systems utilizing chromatic focal shifts, resulting in significant SNR degradation, similar to the limitations of Bessel beam OCT. Moreover, many of these studies overlook a comprehensive analysis of the performance effects of chromatic focal shifts, including their influence on axial resolution and SNR. Conversely, other studies focus on minimizing chromatic focal shifts to prevent deterioration of axial resolution [29–32]. These contradictory approaches highlight the lack of a unified framework and emphasize the need for detailed performance analysis and optimization in research on chromatic focal shifts in OCT.

To address these challenges, we developed a novel OCT system that incorporates three key features to capitalize on the benefits of the axial chromatic focal shift while minimizing its potential drawbacks. First, our system utilizes sample arm optics with a significant chromatic focal shift and a high NA to extend the DOF while maintaining a high lateral resolution. Second, it employs a broad bandwidth light source and a detector to ensure a high axial resolution. Third, we developed a specialized algorithm that effectively reduces noise and mitigates artifacts, optimizing the overall system performance. This system, which we term chromatic OCT, achieves an isotropic high resolution of 2 to 3 μm and demonstrates up to a sevenfold enhancement in the DOF. We validated the effectiveness of chromatic OCT through detailed imaging simulations and comparative performance evaluations against conventional high-resolution OCT systems. Additionally, we compared the proposed chromatic OCT with Bessel beam OCT in terms of the resolution, SNR, and DOF gain. High-resolution imaging experiments with biological tissues further showcase the advantages of chromatic OCT, revealing its high SNR and minimal artifacts across an extended imaging range.

2. METHODS

A. Chromatic OCT System

The chromatic OCT system described in this study utilizes a spectral domain OCT framework [33], incorporating several distinct features designed to induce chromatic focal shifts, as depicted in Fig. 1. The system utilizes light from a supercontinuum laser (SC400, Fianium, Southampton, UK), which is filtered through a short-pass filter (FESH0950, Thorlabs, Newton, NJ, USA) and a long-pass filter (FELH0650, Thorlabs), to provide broadband illumination over a spectral range of 650 to 950 nm, achieving high axial resolution and wide chromatic focal shift (see Appendix A for details). The light is then directed into a 2 × 2 fiber coupler (TW850R5A2, Thorlabs) and subsequently split into the sample and reference arms. In the sample arm, a pair of dispersive lenses (16-975, Edmund Optics, Barrington, NJ, USA) is positioned before the scanning mirror (GVS011/M, Thorlabs). This arrangement produces diverging and converging beams for longer and shorter wavelengths, respectively, while keeping the beam collimated at the center wavelength. These beams then pass through the scanning mirror and a high NA objective lens (DIN Achromatic 10×/0.25 NA, Edmund Optics), focusing at various axial positions to create a narrow and elongated focus, establishing an effective NA of 0.08. In the reference arm, a custom-designed dispersion compensator is installed, consisting of a glass plate made from the same material as the dispersive lenses used in the sample arm, with a thickness precisely double that of the dispersive lenses to ensure matched dispersion characteristics between the two arms. To account for any residual dispersion mismatch, we applied digital compensation during postprocessing by measuring the spectral phase using a mirror and applying a numerical phase correction in the wavenumber domain. The interference signal is detected by a spectrometer (Cobra 800, Wasatch Photonics, Morrisville, NC, USA), covering a bandwidth of 300 nm, ranging from 650 to 950 nm. The spectrometer is equipped with 4096 pixels,

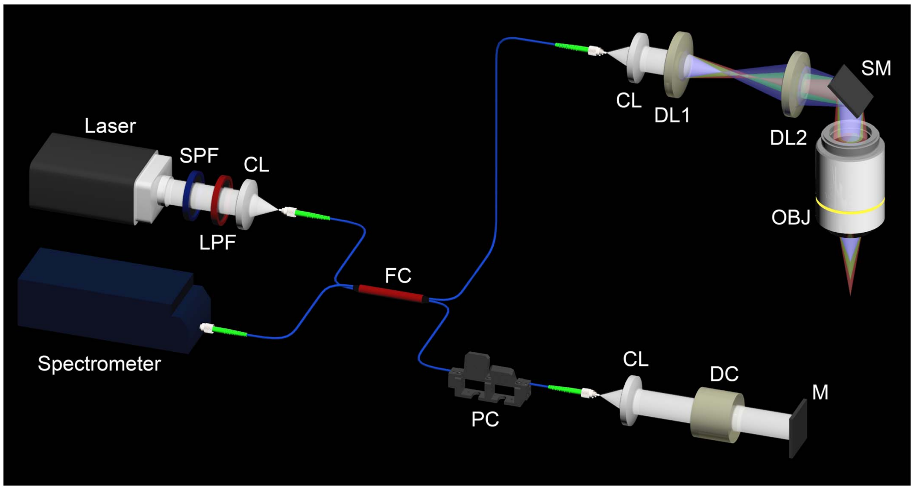

Fig. 1. Schematic diagram of the chromatic OCT system setup. The system utilizes dispersive lenses in the sample arm and a high-NA objective lens to achieve an extended DOF. A broad bandwidth light source (650–950 nm) is used to maintain a high axial resolution. SPF, short-pass filter; LPF, long-pass filter; CL, collimating lens; FC, fiber coupler; DL, dispersive lens; SM, scanning mirror; OBJ, objective lens; PC, polarization controller; DC, dispersion compensator; M, mirror.

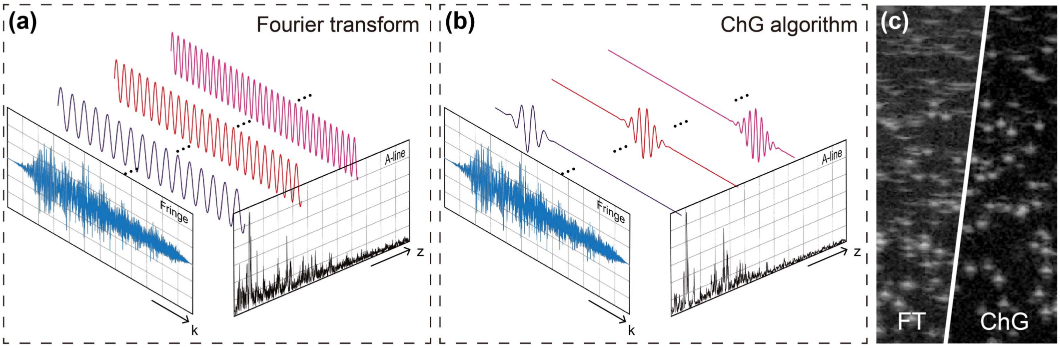

Fig. 2. FT and ChG algorithm. (a) Illustration of signal processing in conventional OCT using the FT. (b) Illustration of the ChG algorithm. This algorithm uses a Gaussian window that shifts according to the frequency of the harmonics, allowing only valid wavenumber regions to be used for image reconstruction and thus reducing noise and artifacts. (c) Comparative bead imaging results using the FT and the ChG algorithm.

resulting in a spectral resolution of 0.073 nm per pixel, allowing for a maximum axial imaging range of up to 2.11 mm in air. The manufacturer-provided calibration data, mapping each pixel to its corresponding wavelength, was used to perform *k*-domain linearization during postprocessing, ensuring accurate depth reconstruction across the full spectral range.

B. ChG Algorithm

We developed and applied a chromatic gating (ChG) algorithm, instead of the conventional FT [Fig. 2(a)], for processing interference signals to resolve artifacts and noise in the proposed chromatic OCT system, as depicted in Fig. 2(b) and detailed in Appendix B. This algorithm leverages the correlation between the depth and the wavenumber of the chromatic OCT system. In conventional OCT systems without a chromatic focal shift, although the interference signals vary in frequency with the sample depth, their envelopes do not correlate with the depth. In contrast, the chromatic focal shift causes these envelopes to shift in the wavenumber domain according to the sample depth. Assuming that the chromatic focal shift is caused by normal dispersion, signals from samples closer to the objective lens show a higher intensity in higher wavenumber (shorter wavelength) regions, and this tendency shifts to lower wavenumber (longer wavelength) regions as the sample distance increases. Outside these regions, only noise is present without valid signals. The FT, typically employed in OCT for image reconstruction, extracts the signals across all wavenumber regions regardless of the sample depth [Fig. 2(a)]. This process is suitable for standard OCT systems, but in systems with significant chromatic focal shift, the conventional FT utilizes both valid and invalid signal regions, leading to unnecessary artifacts and noise. The proposed ChG algorithm addresses this issue by adding a Gaussian window that is variably centered, shifting in accordance with the frequency of the harmonics [Fig. 2(b)]. This allows only the valid wavenumber regions that are in focus to be used for image extraction, thereby reducing excessive noise. Through this wavenumber-based filtering mechanism, the ChG algorithm mitigates three types of noise. First, it effectively suppresses system-inherent noise while minimizing signal loss. Second, it mitigates sidelobe artifacts arising from spectral components that are focused at nontarget depths due to chromatic focal shifts. Third, the algorithm filters out multiple scattered light, which typically travels along extended optical path lengths and interferes with signals from deeper tissues, creating noise. These improvements result in increased SNR and enhanced visualization of deeper tissue structures. Bead imaging results [Fig. 2(c)] briefly demonstrate the effectiveness of the ChG algorithm over the conventional FT-based image reconstruction algorithm.

3. RESULTS

A. Numerical Analysis and Validation

Optical modeling software, Optics Studio (Zemax), was utilized to simulate the output beam characteristics of our customized sample arm. Figure 3(a) illustrates the illumination point spread functions (PSFs) at various wavelengths. Additionally, Fig. 3(b) displays the axial positions of the focal points as a function of the wavelength, revealing a total chromatic focal shift of 487 μm in the sample arm.

For a comprehensive assessment of the system performance beyond what optical modeling software can provide, we designed and executed an OCT imaging simulation that covers the entire OCT imaging process. This includes (1) illumination and detection via the sample arm, (2) illumination and detection via the reference arm, (3) the generation of the interference signal, (4) the ChG algorithm for chromatic OCT (FT for conventional OCT), and (5) lateral scanning (see Appendix C for details). In the sample arm simulation, we incorporated wavelength-dependent focal lengths to account for the chromatic focal shift. The simulations were performed with a spectral range of 650 to 950 nm and an effective NA of 0.08. The chromatic focal shift was set to 487 μm for the chromatic OCT, matching the parameters used in the experimental setup.

The simulated interference patterns of single scattering objects are shown in Fig. 10 of Appendix C. These patterns demonstrate that the envelope of the interference pattern in chromatic OCT is narrower than in conventional OCT. Moreover, as the scattering object moves away axially, the envelope in chromatic OCT shifts accordingly, unlike in conventional OCT, where the envelope remains static, as previously noted. To account for system-inherent noise, we incorporated noise into the simulation (Fig. 11 of Appendix C), numerically demonstrating the ChG algorithm's ability to

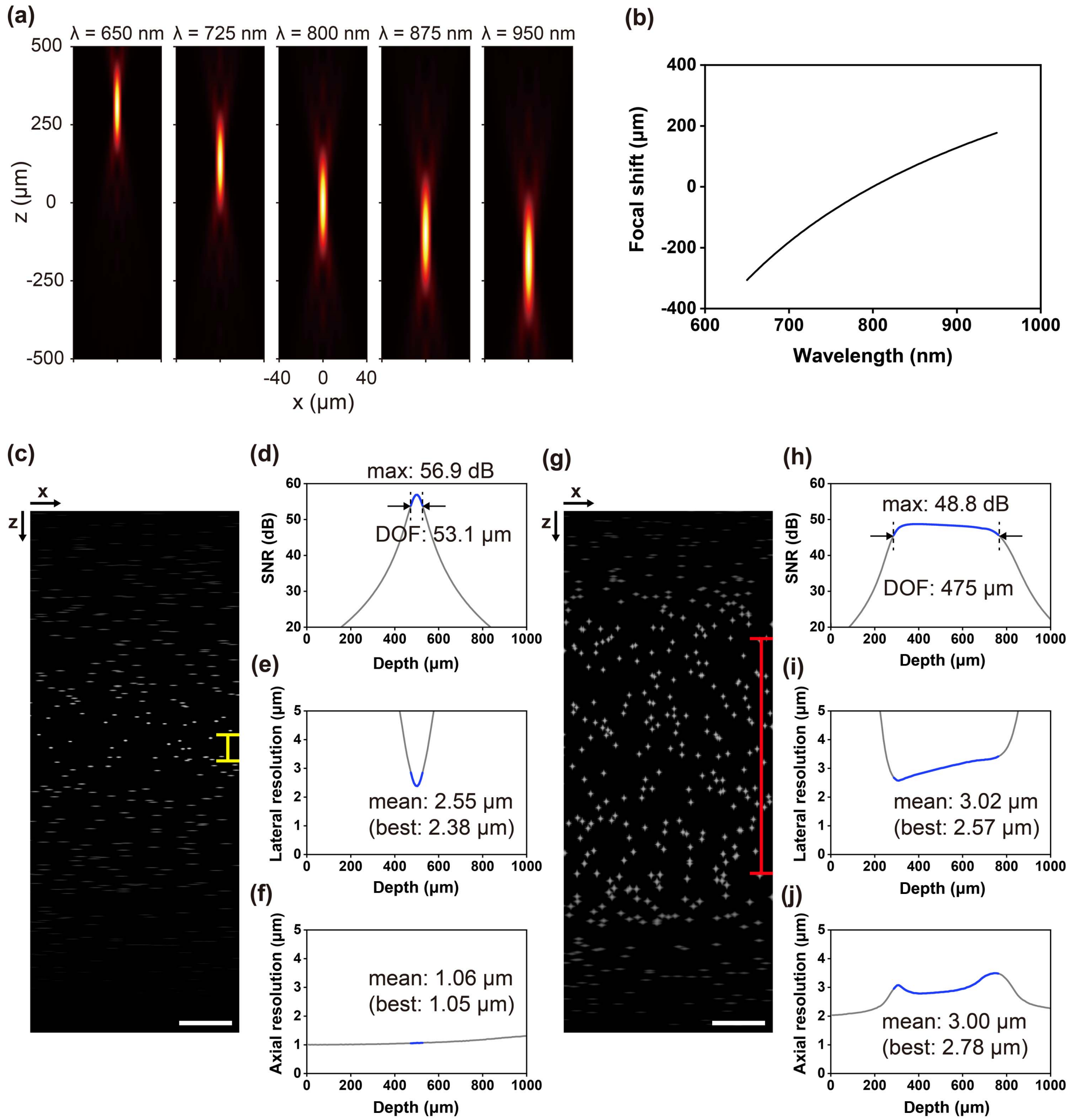

Fig. 3. Numerical analysis of the system performance. (a) PSFs of the sample arm at various wavelengths, generated using optical modeling software. (b) Axial positions of focal points across different wavelengths, demonstrating a total chromatic focal shift of 487 μm. (c) Simulated bead imaging with conventional high-resolution OCT, showing blurring beyond 50 μm from the focal plane. The DOF is indicated by the yellow bar on the right. (d) SNR, (e) lateral resolution, (f) axial resolution as a function of the depth for conventional high-resolution OCT. (g) Simulated bead imaging with chromatic OCT, maintaining a high resolution and SNR over an extended depth range. The DOF is indicated by the red bar on the right. (h) SNR, (i) lateral resolution, (j) axial resolution as a function of the depth for chromatic OCT. Scale bars, 100 μm.

enhance SNR. The reconstructed A-line from the ChG algorithm highlighted a significant noise reduction of −5.46 dB compared to the FT, while the signal intensity experienced only a minimal loss of about −2.1 dB. Ultimately, this resulted in an overall SNR improvement of 3.36 dB.

Figures 3(c) and 3(g) display the bead imaging simulation results for conventional high-resolution OCT (with FT) and chromatic OCT (with ChG algorithm), respectively, under identical conditions except for the chromatic focal shift. In conventional high-resolution OCT, immediate blurring of beads displaced approximately 50 μm from the objective lens's focal plane was observed, whereas chromatic OCT maintained high-resolution, high-contrast images over an axial range of approximately 500 μm. System performance for both scenarios was numerically analyzed in terms of the SNR, lateral resolution, and axial resolution as a function of the imaging depth [Figs. 3(d)–3(f) and 3(h)–3(j)] (see Appendix D for details). Consistent with the observations in Figs. 3(c) and 3(g), chromatic OCT demonstrated a significantly extended DOF of 475 μm compared to the conventional high-resolution OCT's outcome of 53.1 μm [Figs. 3(d) and 3(h)], maintaining a high lateral resolution throughout the enhanced DOF [Figs. 3(e) and 3(i)]. However, there was a notable degradation in axial resolution due to the decreased effective bandwidth

Table 1. Comparison of Simulated Performance Outcomes of Conventional High-resolution OCT and Chromatic OCT

	High-resolution OCT	Chromatic OCT
DOF (μm)	53.1	**475**
PSNR (dB)	56.9	**48.8**
Mean lateral resolution (μm)	2.55	**3.02**
Mean axial resolution (μm)	1.06	**3.00**

of the interference signal [Figs. 3(f) and 3(j)]. Nonetheless, employing a light source with an ample spectral bandwidth ensured that the reduced axial resolution remains comparable to the lateral resolution, allowing the system to achieve an isotropic resolution of 3 μm. Although the peak SNR of chromatic OCT is reduced compared to conventional high-resolution OCT, it maintains a high SNR across a significantly extended depth range. These pivotal performance metrics are summarized and compared in Table 1.

Further, simulations were iteratively conducted while varying the chromatic focal shift and plotting the performance metrics against the amount of chromatic focal shift in Figs. 4(a) and 4(b). Notably, as the chromatic focal shift increases, the DOF gain (the ratio between the DOFs of chromatic and conventional OCT) also increases. However, this is accompanied by reductions in the peak SNR and axial resolution, whereas the lateral resolution remains relatively unaffected.

The performance of chromatic OCT was also compared with that of Bessel beam OCT [Figs. 4(c) and 4(d)], focusing on the SNR penalty, defined as a reduction of the peak SNR, and the axial resolution, both evaluated in relation to the DOF gain. For Bessel beam OCT, the SNR penalty and DOF gain were quantified by the following formulas from a previous report [26]:

$$\text{SNR penalty (dB)} = 20\log\left(\frac{1.213}{N}\right), \tag{1}$$

$$\text{DOF gain} = 1.26N, \tag{2}$$

where N is the Fresnel number. We presumed the axial resolution of Bessel beam OCT to be equivalent to that of standard OCT. This comparison highlighted chromatic OCT's enhanced SNR, despite a considerable compromise in axial resolution compared to Bessel beam OCT.

B. Experimental Performance Evaluation

We experimentally characterized the developed chromatic OCT system through a bead imaging experiment. To ensure an unbiased comparison, our experimental setup was designed to allow easy switching between chromatic OCT and conventional high-resolution OCT configurations. This was achieved by selectively including or excluding specific dispersive optical elements, specifically a pair of dispersive lenses and a dispersion compensator. Such adaptability ensured that both systems could be evaluated under identical experimental conditions, allowing for a direct and equitable comparison of their performance metrics. Figure 5 presents the imaging outcomes of

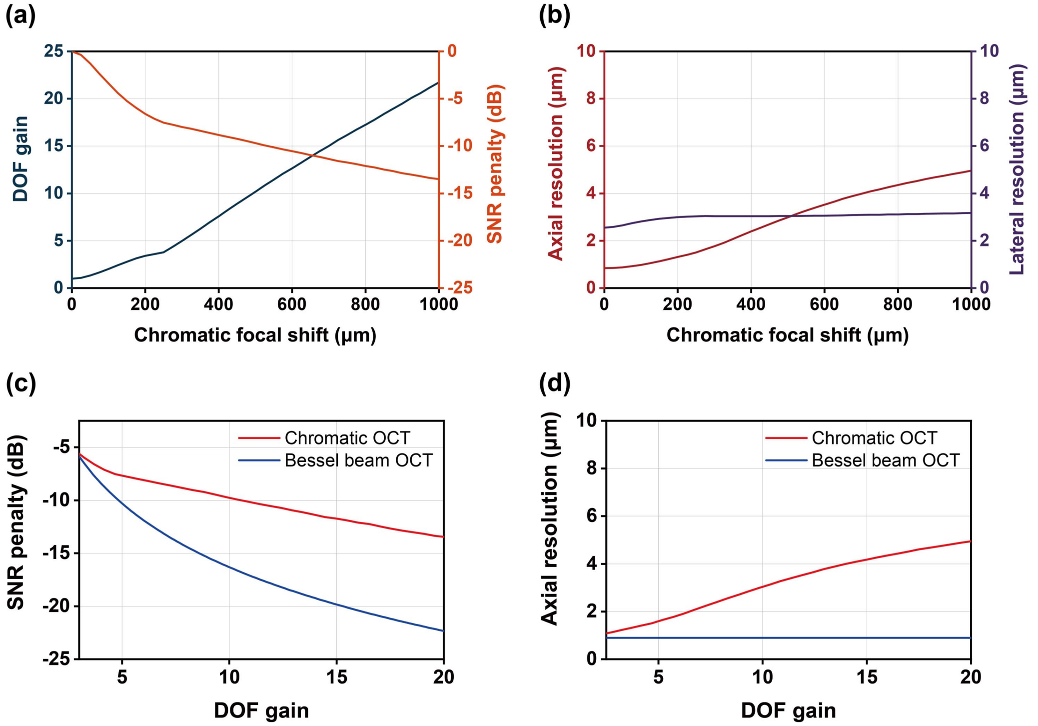

Fig. 4. System performance with varying chromatic focal shift and comparison with Bessel beam OCT. (a) DOF gain, SNR penalty, (b) axial resolution and lateral resolution versus the chromatic focal shift length. Comparison of (c) the SNR penalty and (d) the axial resolution versus DOF gain between chromatic OCT and Bessel beam OCT.

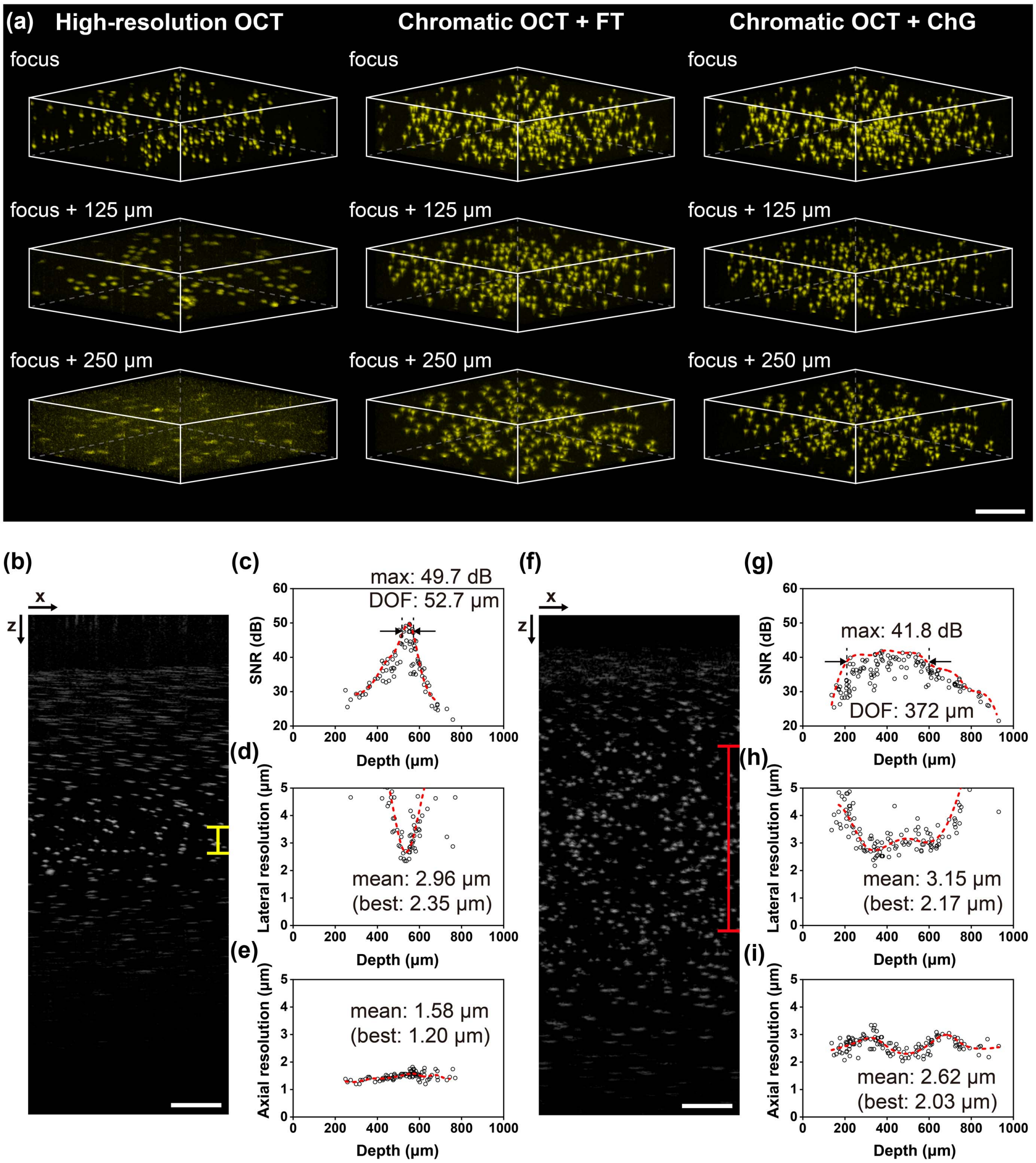

Fig. 5. Experimental system characterization through bead imaging. (a) 3D-rendered images of 0.99 μm polystyrene beads in water obtained using conventional high-resolution OCT, chromatic OCT with the FT, and chromatic OCT with the ChG algorithm. (b) Cross-sectional B-scan image of beads using conventional high-resolution OCT. The DOF is indicated by the yellow bar on the right. (c) SNR, (d) lateral resolution, (e) axial resolution as a function of the depth for conventional high-resolution OCT. (f) Cross-sectional B-scan image of beads using chromatic OCT. The DOF is indicated by the red bar on the right. (g) SNR, (h) lateral resolution, (i) axial resolution as a function of the depth for chromatic OCT. In (c)–(e) and (g)–(i), red dashed lines represent trend curves obtained by dividing the depth range into intervals, extracting either the maximum (for SNR) or mean (for resolution) value within each interval, and then applying spline interpolation to visualize the depth-dependent performance. Scale bars, 100 μm.

polystyrene microbeads, each with a diameter of 0.99 μm, suspended in water. Specifically, Fig. 5(a) provides 3D-rendered images from conventional high-resolution OCT, chromatic OCT using an FT algorithm, and chromatic OCT enhanced with a ChG algorithm. In the conventional OCT imaging, while beads closer to the focus are depicted with clarity, those farther from the focus exhibit noticeable blurring. Beads at a distance of 125 μm from the focus are blurred twice as much, and at 250 μm, they become indiscernible. In contrast, chromatic OCT maintains clear visualization of beads even when they are 250 μm away from the focus. Notably, the application of the ChG algorithm effectively mitigates the blurring effect and significantly enhances the SNR compared to the FT.

Figures 5(b) and 5(f) correspondingly present cross-sectional B-scan images of the beads using conventional high-resolution OCT (with FT) and chromatic OCT (with ChG algorithm). These results validate the simulated trends observed in Figs. 3(c) and 3(g), demonstrating strong agreement between numerical predictions and experimental measurements. In line with our numerical analysis, we assessed the performance of

Table 2. Comparison of Experimentally Evaluated Performance Outcomes of Conventional High-resolution OCT and Chromatic OCT

	High-resolution OCT	Chromatic OCT
DOF (μm)	52.7	**372**
PSNR (dB)	49.7	**41.8**
Mean lateral resolution (μm)	2.96	**3.15**
Mean axial resolution (μm)	1.58	**2.62**

each system across various imaging depths in terms of the SNR, lateral resolution, and axial resolution, employing the same methodology. These results, presented in Figs. 5(c)–5(e) and 5(g)–5(i), consistently align with the trends observed in the simulation results, described in Fig. 3. The slight axial resolution degradation observed in Fig. 5(e), relative to the theoretical value, is likely caused by the finite bead size of 0.99 μm, with a minor possible contribution from residual dispersion. The comparative data compiled in Table 2 highlight that the DOF achieved by chromatic OCT is more than sevenfold greater than that of conventional OCT. Additionally, within this extended DOF, both lateral and axial resolutions were maintained at high levels, averaging 3.15 and 2.62 μm, respectively. Although the peak SNR decreased by 7.9 dB, chromatic OCT achieved a higher SNR over a broader depth range, making it a favorable trade-off for extended-depth imaging, as shown in Fig. 5(f).

Furthermore, the effectiveness of the ChG algorithm was directly compared to the FT method using the same data set from the chromatic OCT system, as demonstrated in the magnified bead images in Fig. 12 of Appendix E. The FT-reconstructed images exhibited wing-like artifacts around the beads, originating from spectral components focused at other depths that contributed undesired signals at the target plane. The ChG algorithm effectively suppressed these artifacts by isolating only the relevant spectral region for each depth. Additionally, ChG reduced system-inherent noise, resulting in a peak signal-to-noise ratio (PSNR) improvement of approximately 2 to 6 dB across all measured depths ($z = 200$, 400, 600, and 800 μm).

C. Tissue Imaging

To demonstrate the practical utility of chromatic OCT, we conducted *ex vivo* imaging experiments on fresh tissue samples using our developed system. Figure 6 presents cross-sectional images of lemon flesh, comparing results obtained with conventional high-resolution OCT and chromatic OCT [Figs. 6(a) and 6(b), respectively]. In the conventional high-resolution OCT images, the cell walls are sharply defined near the focal plane [Fig. 6(a2)] but appear blurred and seemingly wider in areas 250 μm away from the focus [Figs. 6(a1) and 6(a3)], as highlighted by the yellow arrows. In contrast, images from chromatic OCT consistently display clear cellular structures throughout, including areas distant from the focal plane, as shown in the magnified views [Figs. 6(b1)–6(b3), red arrows].

Figures 7(a) and (b) show cross-sectional chromatic OCT images of freshly excised swine esophagus mucosal tissue, processed with the ChG algorithm [Fig. 7(a)] and the conventional FT algorithm [Fig. 7(b)] using identical data sets, revealing cellular structures that closely corroborate with the H&E histology section [Fig. 7(c)]. The ChG-processed image [Fig. 7(a)] exhibits significantly enhanced image quality, especially in visualizing mature squamous epithelial cells having abundant glycogen in cytoplasm, compared to the FT-processed image [Fig. 7(b)]. Magnified views of epithelial cells at three different depths [Fig. 7(d)] further demonstrate the ChG algorithm's effectiveness in deep tissue imaging. Axial depth profiles along the dashed lines highlight the superior contrast achieved by the ChG algorithm, revealing structures that were previously noisy or indistinct with the FT algorithm. To quantify this enhancement, contrast analyses were conducted on 10 individual cells (see Fig. 13 of Appendix F), including those shown in Fig. 7(d). We marked each cell's boundary to compare the average intensities inside and outside these contours. The resulting contrast

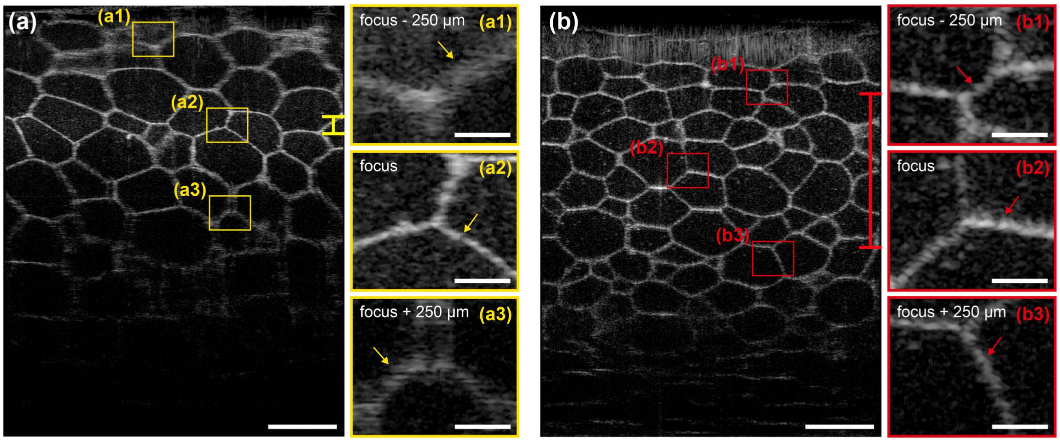

Fig. 6. *Ex vivo* imaging of lemon flesh. (a) Cross-sectional image of lemon flesh using conventional high-resolution OCT, showing blurred cell walls at depths away from the focal plane. The DOF is indicated by the yellow bar on the right. Magnified views [(a1)–(a3)] highlight blurring in the defocus area. (b) Cross-sectional image using chromatic OCT, displaying clear cell walls throughout the imaging range. The DOF is indicated by the red bar on the right. Magnified views [(b1)–(b3)] demonstrate consistent clarity even at a distance of 250 μm away from the focal plane. Scale bars for (a) and (b), 200 μm. Scale bars for (a1)–(a3) and (b1)–(b3), 40 μm.

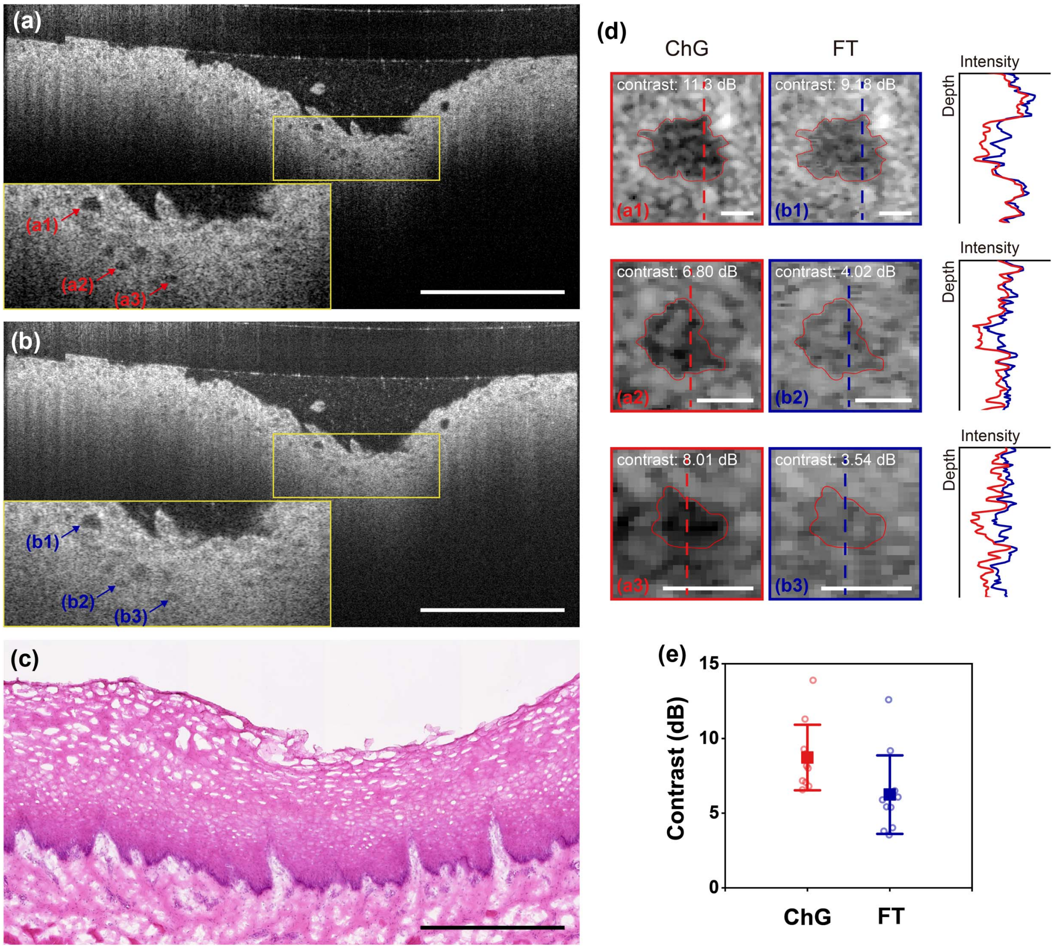

Fig. 7. *Ex vivo* imaging of swine esophagus. (a) Cross-sectional image of a swine esophagus using chromatic OCT with the ChG algorithm, clearly identifying glycogen-rich squamous epithelial cells. (b) Cross-sectional image using chromatic OCT with the conventional FT, showing more noise and less clarity of the cellular structures. (c) Representative H&E histology image corresponding to (a) and (b). (d) Magnified images of epithelial cells from (a) [(a1)–(a3)] and (b) [(b1)–(b3)]. Depth profiles along the dashed lines are shown on the right [(a1)–(a3) in red and (b1)–(b3) in blue]. (e) Contrast analysis for 10 individual cells, comparing the inner and surrounding regions for each cell in (a) and (b). Each circular point represents the contrast values for a distinct cell, with the mean and standard deviation plotted to summarize the contrast enhancement achieved by the ChG algorithm relative to FT. Scale bars for (a)–(c), 500 μm. Scale bars for (d), 15 μm.

data, summarized in Fig. 7(e), show that the ChG algorithm achieved a mean contrast of 8.72 dB (standard deviation 2.19 dB), surpassing the FT's mean of 6.24 dB (standard deviation 2.62 dB). This 2.48 dB improvement, corresponding to a 39.7% increase in mean contrast, is particularly significant for deep tissue imaging, where the contrast is typically limited to just a few decibels. This enhancement highlights the ability of the ChG algorithm to effectively suppress multiple scattered light and noise within highly scattering tissues.

Figure 8 presents imaging results from a freshly excised swine stomach acquired by the chromatic OCT system and the ChG algorithm. The 3D-rendered image [Fig. 8(a)], en face image [Fig. 8(b)], and cross-sectional B-scan image [Fig. 8(c)] collectively demonstrate the 3D architecture of the mucosal surface composed of gastric glands and pits with remarkable clarity, a finding confirmed by the corresponding H&E histology section [Fig. 8(d)]. Additionally, Visualization 1 demonstrates the system's capabilities by navigating through various cross-sectional and en face views, providing a detailed visualization of the tissue structures, specifically the high intensity signal in the gastric epithelial cells and the relatively low intensity signal in the lamina propria, composed of loosely connective tissue. The intracellular organelles of gastric glandular epithelial cells display a high intensity signal with granularity compared to the esophageal squamous epithelial cells. This comprehensive display of images and the corresponding video highlights the system's advanced resolution and clarity, demonstrating its potential for detailed analysis of complex tissue structures. It suggests high effectiveness when combined with endoscopic examination for detecting the gross architecture and mucosal surface alterations accompanying various benign or malignant tumors in the gastrointestinal tract.

4. DISCUSSION

Achieving a high resolution in conjunction with an extended DOF is a critical development in the field of OCT that addresses one of the most challenging aspects in biomedical

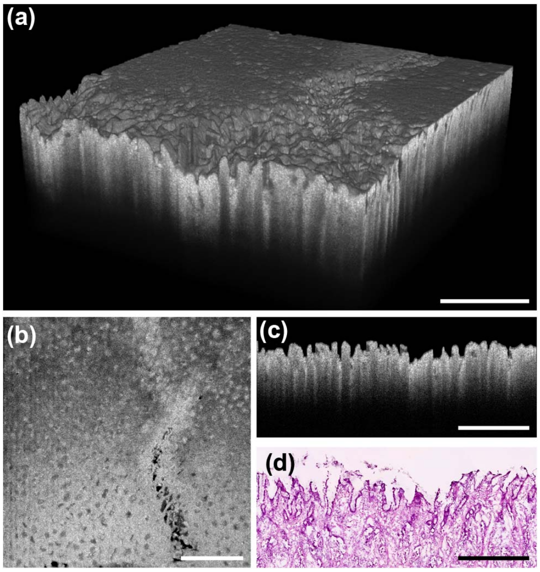

Fig. 8. *Ex vivo* imaging of swine stomach. (a) 3D-rendered image, (b) en face image, (c) cross-sectional image, and (d) representative H&E histology image of a swine stomach acquired by chromatic OCT, revealing detailed 3D architecture of gastric glandular pits. The en face and cross-sectional images demonstrate relatively high intensity signal of the gastric epithelium compared to the lamina propria area composed of loosely connective tissue. Scale bars, 500 μm.

imaging. This study proposes a straightforward and effective method to resolve the inherent trade-off between a high lateral resolution and the DOF by introducing intentional chromatic focal shifts. While previous studies utilized chromatic focal shifts to enhance the DOF [27,28], the development of appropriate image reconstruction algorithms for such systems, as well as comprehensive investigations into how these shifts quantitatively impact the overall system performance, has been notably absent. This study fills this gap by introducing a ChG algorithm designed specifically for OCT systems that employ chromatic focal shifts. Through noise-included simulations, bead imaging, and tissue imaging, we verified that the ChG algorithm effectively reduces system-inherent noise, sidelobe artifacts, and noise from multiple scattering. These advancements establish the ChG algorithm as an additional gating mechanism, enhancing traditional coherence and confocal gating and thereby significantly improving the image quality.

Through detailed OCT imaging simulations, we quantitatively assessed the impact of chromatic focal shifts on imaging performance metrics, including DOF, lateral resolution, axial resolution, and SNR. The results confirmed that chromatic OCT provides a distinct advantage in terms of the SNR compared to the commonly used Bessel beam OCT. Furthermore, unlike various computational methods [14,15] that require phase stability, the chromatic OCT approach operates regardless of such constraints, indicating its robust applicability across diverse imaging scenarios. Consequently, chromatic OCT uniquely satisfies the requirements for high-resolution, extended DOF, high SNR, and robustness, positioning it as a superior method for high-resolution deep tissue imaging applications.

However, utilizing chromatic focal shifts leads to a reduction of the effective bandwidth, consequently diminishing the axial resolution. Therefore, to maintain a high axial resolution comparable to the lateral resolution, it is essential to utilize a light source with a sufficiently broad bandwidth, as demonstrated in this study. It is noteworthy that in most high-resolution OCT systems, the axial resolution generally surpasses lateral resolution, often reaching submicrometer levels, whereas the lateral resolution is typically limited to a few micrometers. Therefore, sacrificing some axial resolution can be a practical strategy to address the fundamental trade-off between lateral resolution and DOF, enabling more isotropic spatial resolution over an extended depth range. Interestingly, Harper *et al.* [34] reported that, in diffusely scattering samples, reduced axial resolution can improve measurement SNR by allowing more backscattered photons to be collected over a broader depth range. In chromatic OCT, reduced effective bandwidth inherently degrades axial resolution and can lower SNR. However, in diffusely scattering samples, this SNR degradation can be mitigated by the same mechanism described in Ref. [34].

A practical consideration in chromatic OCT is the spectral nonuniformity of the light source, which may cause signal intensity variations across different depths. Although normalization using a reference spectrum reduces spectral bias, residual SNR variation can still persist. In addition, wavelength-dependent scattering and absorption in biological tissue can also introduce spectral distortion. However, in most cases, longer wavelengths inherently scatter less, and when combined with chromatic focal shifts that bring these wavelengths into focus at greater depths, this characteristic may help enhance tissue penetration and potentially improve SNR.

It is also important to note that the chromatic focal position for each wavelength can vary in practice, primarily due to changes in imaging conditions, particularly the distance between the objective lens and the sample surface. In the ChG algorithm, this variation may shift the appropriate location of the window function applied during reconstruction. To address this, the window position was manually adjusted for each imaging condition based on a qualitative assessment of the reconstructed images. Future improvements could include automated optimization schemes to improve reproducibility and reduce user dependency.

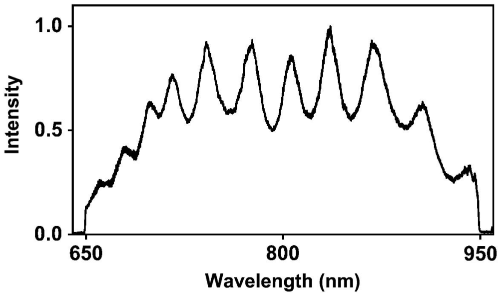

Fig. 9. Measured spectrum of the light reflected from the reference mirror with the sample arm left empty. The spectrum spans the 650–950 nm range and is normalized to its peak intensity.

APPENDIX A: MEASURED SPECTRUM AT THE DETECTOR

To confirm the spectral shape used in the system, we measured the light spectrum reflected from the reference mirror with the sample arm left empty, as shown in Fig. 9. The spectrum spans the 650–950 nm range but is nonuniform due to several factors: the intrinsic output profile of the supercontinuum light source, the wavelength-dependent responsivity of the detector, and transmission losses within the interferometer. During post-processing, this reference spectrum was used to normalize the interferograms and minimize spectral bias in image reconstruction.

APPENDIX B: IMPLEMENTATION DETAILS OF THE ChG ALGORITHM

For the conventional OCT system, the image reconstruction algorithm employs the following inverse discrete FT formula:

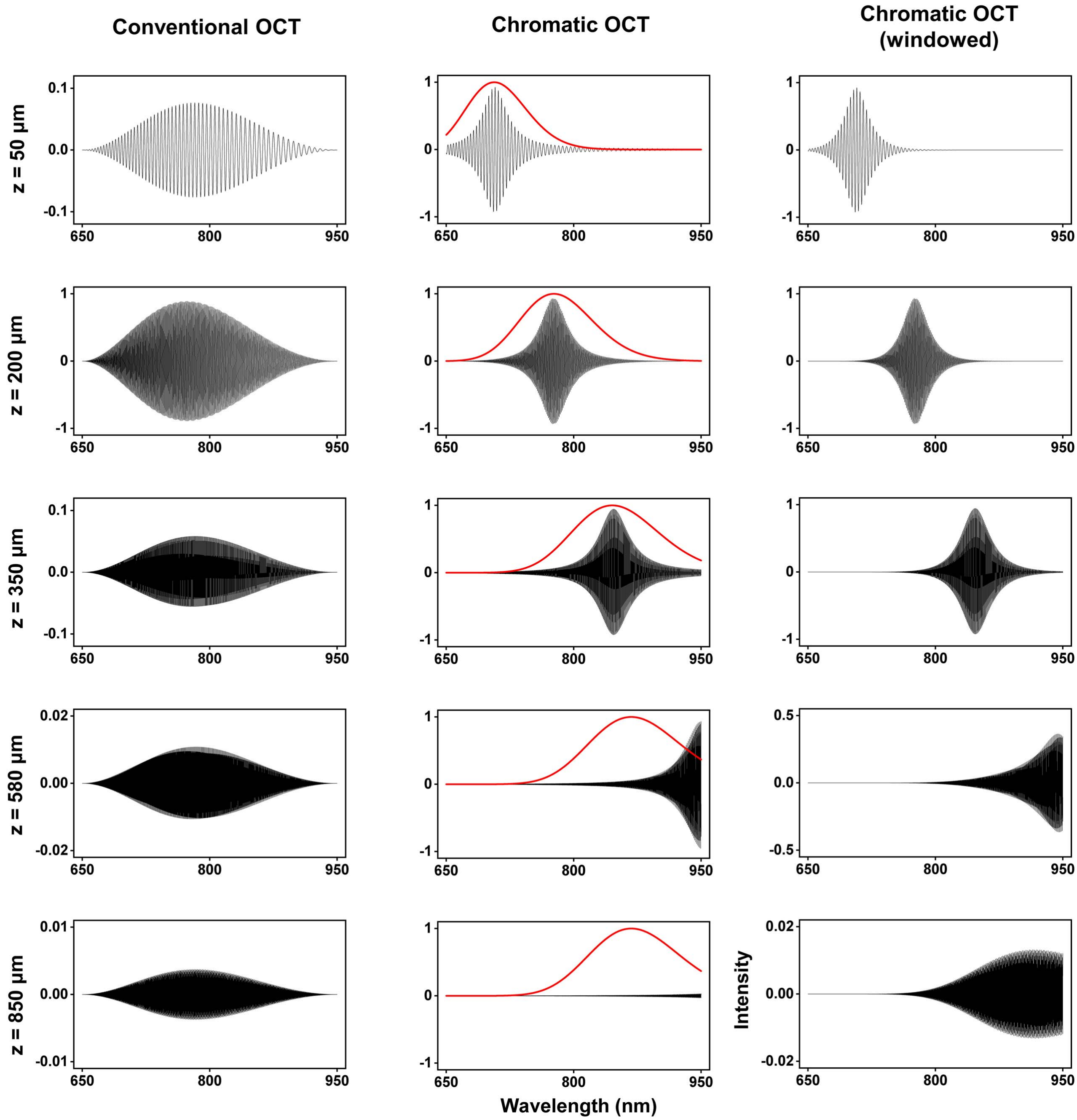

Fig. 10. Simulated interference signal of single scattering objects at various axial depths ($z = 50$, 200, 350, 580, and 850 μm) in conventional and chromatic OCT systems. The first column shows the interference signals for conventional OCT, windowed with a Hanning function for clarity. The second column presents chromatic OCT fringes at corresponding depths, overlaid with red Gaussian windows employed in the ChG algorithm. The third column displays the chromatic OCT fringes after applying the corresponding Gaussian windows. Note that the intensity range of each graph is different.

$$i[z_m] = \sum_{n=1}^{N} I[k_n] e^{\frac{i k_n z_m}{N}}, \tag{B1}$$

where $I[k_n]$ represents the interference signal, which results from the dispersion compensation and k-linearization algorithm applied to the detected signal from the spectrometer, and $i[z_m]$ is the reconstructed depth profile.

In the ChG algorithm, Gaussian windows ($W[k_n, z_m]$) are incorporated, as follows:

$$i[z_m] = \sum_{n=1}^{N} I[k_n] W[k_n, z_m] e^{\frac{i k_n z_m}{N}}, \tag{B2}$$

$$W[k_n, z_m] = e^{-\frac{1}{2}\left(\frac{k_n - k_c}{\sigma_k}\right)^2}, \tag{B3}$$

$$k_c = \frac{2\pi}{f^{-1}(z_m)}. \tag{B4}$$

Here, k_c represents the center position of the Gaussian windows, and σ_k denotes their width. The function $z_m = f(\lambda_m)$ signifies the axial position of the focus created by the beam at wavelength λ_m, meaning that k_c is the wavenumber of the beam focused at axial position z_m. The function $f(\lambda_m)$ can be derived through three different approaches: optical modeling software as shown in Fig. 3(b), experimental measurements from the system, or manual adjustments based on a visual evaluation of the final images produced by the algorithm. This flexibility allows for precise tuning to optimize the image quality.

In our implementation, we manually adjusted the spectral focus profile, as it varied with the distance between the objective lens and the sample surface. The total chromatic focal shift was estimated from Zemax modeling, and we assumed a linear relationship between wavenumber and axial focus to simplify the model. As a result, the model required only two tunable parameters: the center depth and the total shift range, which were optimized by visual inspection. To verify the validity of this linear approximation, we quantified the deviation between the ideal center positions obtained from simulation and those predicted by linear fitting. The average deviation was 0.031 μm^{-1} in the wavenumber domain, corresponding to only 4.59% of the applied window width (0.667 μm^{-1}). This small deviation indicates that the linear model provides sufficient accuracy for our implementation, especially given the use of broad spectral windows.

In addition, to avoid artifacts caused by spectral truncation near the boundaries of the chromatic focal shift, we constrained the Gaussian window center to remain at least one Gaussian radius away from the boundaries of the k-domain.

For runtime evaluation, the ChG algorithm was tested on a 2D data set consisting of 2000 A-lines and 2048 depth

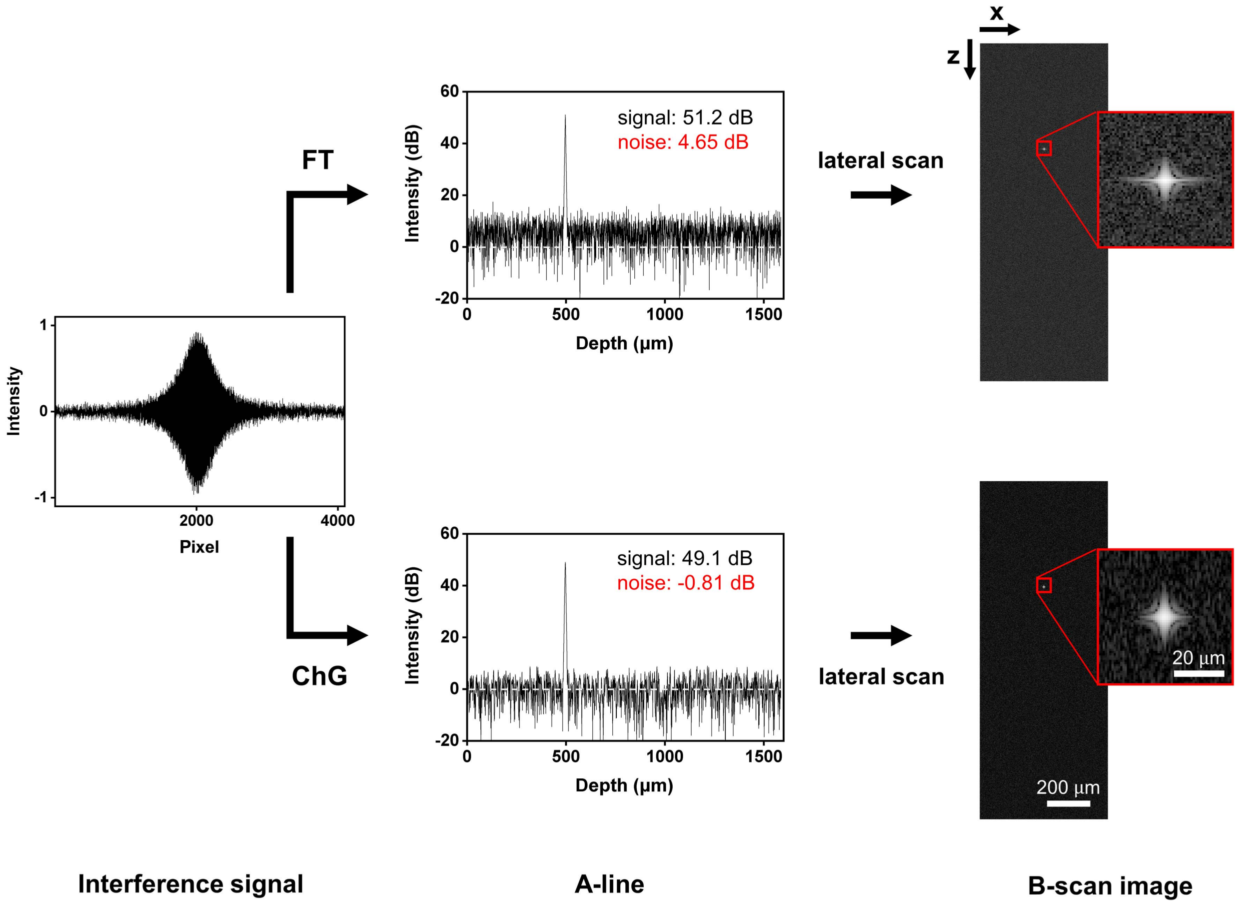

Fig. 11. Comparison between the ChG algorithm and the FT using a noise-included interference pattern from the simulation. FT and ChG algorithm were applied to reconstruct A-line profiles from simulated interference signals of chromatic OCT.

points using a CPU-based MATLAB implementation (AMD Ryzen 5 5600X, 6-core processor). The ChG algorithm required approximately 0.49 s, compared to 0.033 s for the conventional FFT-based method (~15× slower). Further speedups are expected with GPU acceleration or a parallelized C++ implementation.

APPENDIX C: IMPLEMENTATION DETAILS OF THE OCT IMAGING SIMULATIONS

To evaluate the performance of the developed system and algorithm, we conducted an OCT imaging simulation. The simulation process involves the following steps.

First, the complex amplitude of the electric field detected from a point scattering object in the sample arm is calculated, considering the confocal effect and assuming that the illumination and detection PSFs are Gaussian beams [35]. This is defined as follows:

$$E_s(x_s, y_s, z_s, k) = F_0\left(A_0 \frac{w_0}{w(z_s, k)} \exp\left(-\frac{x_s^2 + y_s^2}{w^2(z_s, k)}\right)\right)^2 \times \exp(-2ikz_s), \quad \text{(C1)}$$

where $w(z,k) = w_0\sqrt{1 + (\frac{z - z_0(k)}{z_R})^2}$ represents the beam width, and $z_0(k)$ is the axial position of focus, which varies with the wavenumber to account for chromatic focal shifts. The wavefront of the Gaussian beam is assumed to be planar, and the scattering potential of the point object is represented by $F_0\delta(x - x_s)\delta(y - y_s)\delta(z - z_s)$.

The complex amplitude of the electric field detected in the reference arm is calculated as shown below,

$$E_{\mathrm{ref}}(k) = A_{\mathrm{ref}} \exp(-2ikz_{\mathrm{ref}}). \quad \text{(C2)}$$

The intensity detected by the detector is the square of the sum of the electric fields from the sample and the reference arms,

$$\begin{aligned} I_{\mathrm{det}}(k) &= |E_s + E_{\mathrm{ref}}|^2 \\ &= |E_s|^2 + |E_{\mathrm{ref}}|^2 + E_s E_{\mathrm{ref}}^* + E_s^* E_{\mathrm{ref}} + n_{\mathrm{shot}}. \end{aligned} \quad \text{(C3)}$$

The shot noise term (n_{shot}), which has variation proportional to the reference arm power, is included to account for system-inherent noise and to analyze the SNR of the system. After removing DC terms, the remaining AC term and noise are expressed as follows:

$$I_{\mathrm{AC}}(k) \propto A_{\mathrm{ref}} F_0\left(A_0 \frac{w_0}{w(z_s, k)} \exp\left(-\frac{x_s^2 + y_s^2}{w^2(z_s, k)}\right)\right)^2 \times \cos(2k(z_{\mathrm{ref}} - z_s)) + n_{\mathrm{shot}}. \quad \text{(C4)}$$

The ChG algorithm (or FT for conventional OCT) is applied to the equation for chromatic OCT to produce the A-line depth profile. By altering the lateral position of the point scatterer and repeating the above processes, a B-scan image is generated.

In the simulation, we assumed an idealized top-hat spectrum, where the spectral amplitude was uniform across the 650–950 nm range.

To model the chromatic focal shift, we considered an optical system exhibiting a focal shift of 487 μm in air across the entire spectral bandwidth (except in Fig. 4). To more accurately reflect the experimental imaging conditions, where the sample is immersed in water, we modeled the water medium as beginning 1 mm beyond the lens surface. Using Snell's law and a refractive index of 1.33, we converted the air-based focal positions into equivalent positions within the water medium.

Figure 10 presents simulated interference fringes for conventional OCT and chromatic OCT, excluding shot noise for clarity. Compared to conventional OCT, chromatic OCT fringes exhibit narrower envelopes and depth-dependent spectral variations due to the chromatic focal shift. Specifically, at $z = 50$, 200, and 350 μm (within the chromatic focal range), the spectral envelope shifts with depth while maintaining its full shape. At $z = 580$ μm (near the edge of the focal range), the fringe spectrum weakens and becomes truncated at the boundary of the k-domain, reducing the effective spectral bandwidth. At $z = 850$ μm (outside the focal range), while the overall fringe intensity decreases significantly, the spectral distribution broadens again.

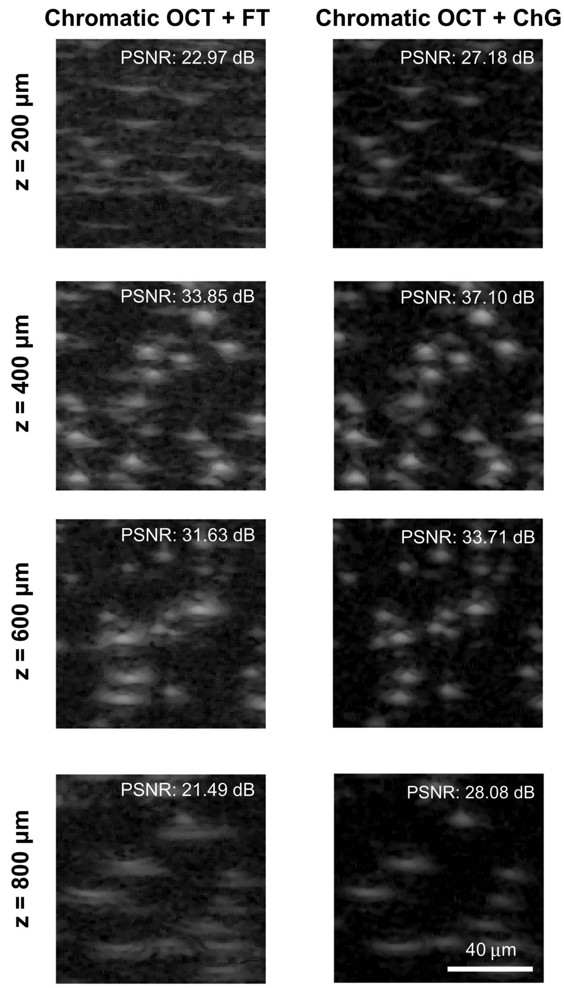

Fig. 12. Comparative analysis between the ChG algorithm and the FT using magnified bead images.

The red Gaussian windows overlaid on the chromatic OCT fringes illustrate how the ChG algorithm handles these variations. As described in Appendix B, the window center shifts with depth to follow the chromatic focal position but is constrained to remain at least one Gaussian radius away from the spectral boundaries to avoid truncation-induced artifacts.

The final windowed fringes help explain the saddle-shaped axial resolution trend observed in Figs. 3(j) and 5(i): the resolution degrades near the edge of the focal range but improves again at depths farther from the focal region.

Figure 11 compares the conventional FT algorithm and the proposed ChG algorithm using noise-inclusive simulations. The maximum signal intensity achieved with the FT algorithm was 51.2 dB, with a noise level of 4.65 dB. In contrast, the ChG algorithm achieved a maximum signal intensity of 49.1 dB while reducing the noise level to −0.81 dB, resulting in an SNR improvement by 3.36 dB.

APPENDIX D: EVALUATION OF SYSTEM PERFORMANCE METRICS

The performance of our OCT system was evaluated through numerical simulations of bead imaging [Figs. 3(d)–3(f) and 3(h)–3(j)] and experimental bead imaging tests [Figs. 5(c)–5(e) and 5(g)–5(i)]. To quantify the system's SNR at various imaging depths [Figs. 3(d), 3(h), 5(c), and 5(g)], we measured and subtracted background noise levels from the peak intensities of individual beads. The lateral resolutions [Figs. 3(e), 3(i), 5(d), and 5(h)] and axial resolutions [Figs. 3(f), 3(j), 5(e), and 5(i)] were determined by analyzing the full width at half-maximum (FWHM) of each bead's intensity profiles in both the lateral

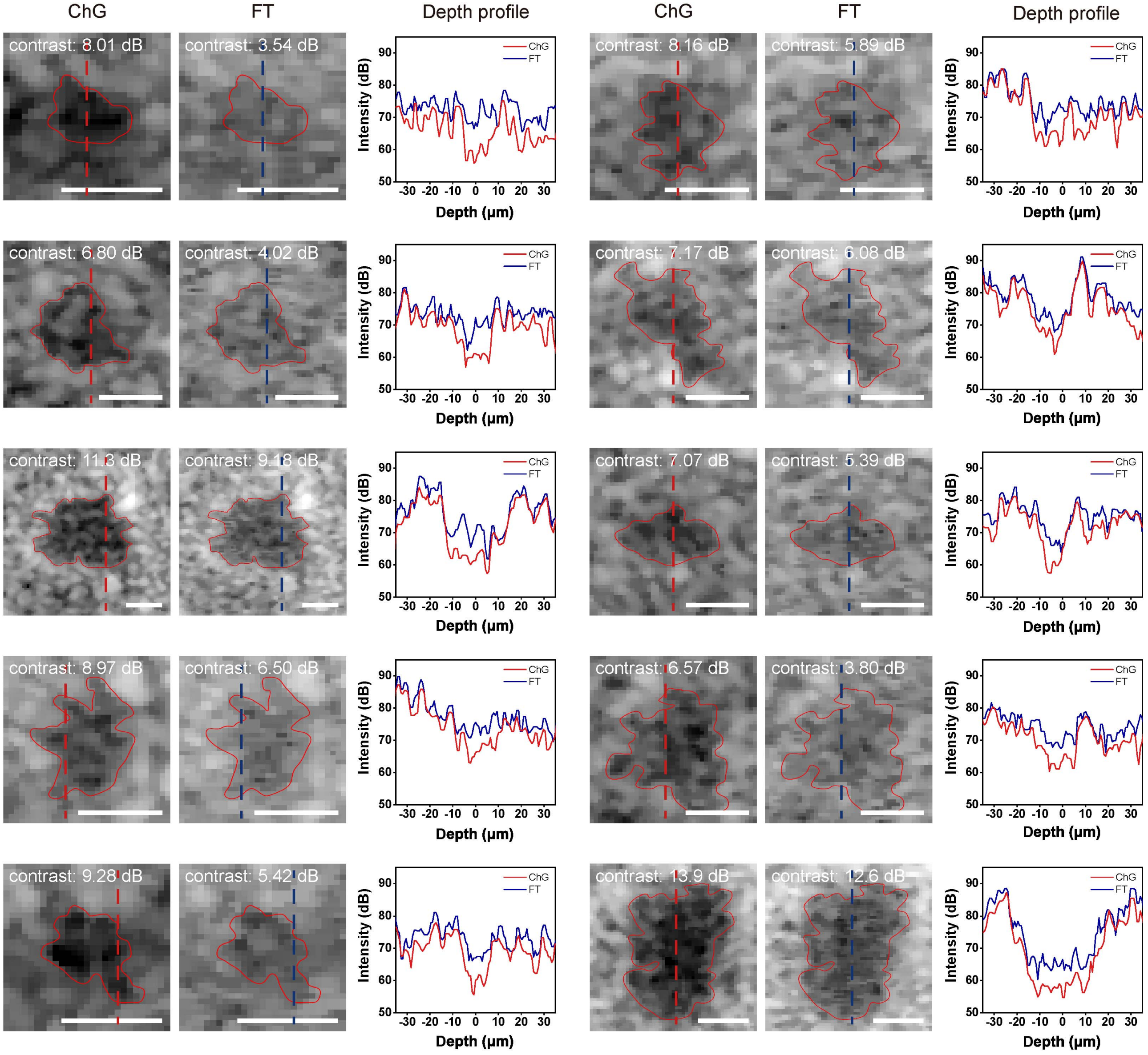

Fig. 13. Comparative analysis between the ChG algorithm and the FT using magnified epithelial cell images in swine esophagus tissue. Scale bars, 15 μm.

and axial directions, respectively. The DOF was ascertained by measuring the axial range in which the SNR remained within 3 dB of its peak value, as defined using the equation below,

$$\mathrm{SNR}(z \in \mathrm{DOF}) \geq \mathrm{SNR}(z = \mathrm{focus}) - 3\ \mathrm{dB}. \tag{D1}$$

Subsequently, we computed the mean and best axial and lateral resolutions within this defined DOF, thereby providing a comprehensive evaluation of the system's imaging performance.

APPENDIX E: MAGNIFIED BEAD IMAGES COMPARING FT AND ChG

Figure 12 displays magnified bead images extracted from Figs. 5(b) and 5(f). Across all examined depths (200, 400, 600, and 800 μm), the images processed with the ChG algorithm exhibit a markedly higher PSNR with improvements of approximately 2 to 6 dB. Moreover, the ChG algorithm significantly reduces sidelobe artifacts, enhancing the clarity and quality of the images.

APPENDIX F: MAGNIFIED EPITHELIAL CELL IMAGES COMPARING FT AND ChG

Figure 13 displays magnified images of epithelial cells, derived from the data set shown in Figs. 7(a) and 7(b), and illustrating the comparative effectiveness of the ChG algorithm versus FT. For each cell, contours were outlined to calculate mean intensities inside and outside the boundary; the resulting contrast was determined by the difference between these measurements. The contrast values, displayed at the top left of each image, are notably higher in the images processed with the ChG algorithm. Depth profiles along the dashed lines further demonstrate the superior clarity and contrast provided by the ChG algorithm.

Funding. National Research Foundation of Korea (RS-2024-00401786, RS-2023-00208888).

Disclosures. S.E.L. and H.Y. are inventors of a patent related to this work filed by the Korea Advanced Institute of Science and Technology (Korean patent application 10-2024-0015151, filed on January 31, 2024). The authors declare no other competing interests.

Data Availability. Representative code and experimental data underlying the results presented in this paper are available in Ref. [36].

REFERENCES

1. D. Huang, E. A. Swanson, C. P. Lin, *et al.*, "Optical coherence tomography," Science **254**, 1178–1181 (1991).
2. G. J. Tearney, M. E. Brezinski, B. E. Bouma, *et al.*, "*In vivo* endoscopic optical biopsy with optical coherence tomography," Science **276**, 2037–2039 (1997).
3. A. M. Rollins, R. Ung-arunyawee, A. Chak, *et al.*, "Real-time *in vivo* imaging of human gastrointestinal ultrastructure by use of endoscopic optical coherence tomography with a novel efficient interferometer design," Opt. Lett. **24**, 1358–1360 (1999).
4. A. M. Zysk, F. T. Nguyen, A. L. Oldenburg, *et al.*, "Optical coherence tomography: a review of clinical development from bench to bedside," J. Biomed. Opt. **12**, 051403 (2007).
5. G. J. Tearney, E. Regar, T. Akasaka, *et al.*, "Consensus standards for acquisition, measurement, and reporting of intravascular optical coherence tomography studies," J. Am. Coll. Cardiol. **59**, 1058–1072 (2012).
6. B. J. Vakoc, D. Fukumura, R. K. Jain, *et al.*, "Cancer imaging by optical coherence tomography: preclinical progress and clinical potential," Nat. Rev. Cancer **12**, 363–368 (2012).
7. W. Drexler, U. Morgner, R. K. Ghanta, *et al.*, "Ultrahigh-resolution ophthalmic optical coherence tomography," Nat. Med. **7**, 502–507 (2001).
8. B. Povazay, K. Bizheva, A. Unterhuber, *et al.*, "Submicrometer axial resolution optical coherence tomography," Opt. Lett. **27**, 1800–1802 (2002).
9. W. Drexler, "Ultrahigh-resolution optical coherence tomography," J. Biomed. Opt. **9**, 47–74 (2004).
10. F. Spöler, S. Kray, P. Grychtol, *et al.*, "Simultaneous dual-band ultra-high resolution optical coherence tomography," Opt. Express **15**, 10832–10841 (2007).
11. L. Liu, J. A. Gardecki, S. K. Nadkarni, *et al.*, "Imaging the subcellular structure of human coronary atherosclerosis using micro–optical coherence tomography," Nat. Med. **17**, 1010–1014 (2011).
12. B. Yin, Z. Piao, K. Nishimiya, *et al.*, "3D cellular-resolution imaging in arteries using few-mode interferometry," Light Sci. Appl. **8**, 104 (2019).
13. J. Kim, S. Kim, J. W. Song, *et al.*, "Flexible endoscopic micro-optical coherence tomography for three-dimensional imaging of the arterial microstructure," Sci. Rep. **10**, 9248 (2020).
14. T. S. Ralston, D. L. Marks, P. S. Carney, *et al.*, "Inverse scattering for optical coherence tomography," J. Opt. Soc. Am. A **23**, 1027–1037 (2006).
15. T. S. Ralston, D. L. Marks, P. Scott Carney, *et al.*, "Interferometric synthetic aperture microscopy," Nat. Phys **3**, 129–134 (2007).
16. X. Yu, X. Liu, J. Gu, *et al.*, "Depth extension and sidelobe suppression in optical coherence tomography using pupil filters," Opt. Express **22**, 26956–26966 (2014).
17. D. Cui, K. K. Chu, B. Yin, *et al.*, "Flexible, high-resolution micro-optical coherence tomography endobronchial probe toward *in vivo* imaging of cilia," Opt. Lett. **42**, 867–870 (2017).
18. L. Liu, C. Liu, W. C. Howe, *et al.*, "Binary-phase spatial filter for real-time swept-source optical coherence microscopy," Opt. Lett. **32**, 2375–2377 (2007).
19. J. Xing, J. Kim, and H. Yoo, "Design and fabrication of an optical probe with a phase filter for extended depth of focus," Opt. Express **24**, 1037–1044 (2016).
20. J. Kim, J. Xing, H. S. Nam, *et al.*, "Endoscopic micro-optical coherence tomography with extended depth of focus using a binary phase spatial filter," Opt. Lett. **42**, 379–382 (2017).
21. Z. Ding, H. Ren, Y. Zhao, *et al.*, "High-resolution optical coherence tomography over a large depth range with an axicon lens," Opt. Lett. **27**, 243–245 (2002).
22. K.-S. Lee and J. P. Rolland, "Bessel beam spectral-domain high-resolution optical coherence tomography with micro-optic axicon providing extended focusing range," Opt. Lett. **33**, 1696–1698 (2008).
23. W. Wang, G. Wang, J. Ma, *et al.*, "Miniature all-fiber axicon probe with extended Bessel focus for optical coherence tomography," Opt. Express **27**, 358–366 (2019).
24. B. Yin, K. K. Chu, C.-P. Liang, *et al.*, "μOCT imaging using depth of focus extension by self-imaging wavefront division in a common-path fiber optic probe," Opt. Express **24**, 5555–5564 (2016).
25. B. Yin, C. Hyun, J. A. Gardecki, *et al.*, "Extended depth of focus for coherence-based cellular imaging," Optica **4**, 959–965 (2017).
26. D. Lorenser, C. C. Singe, A. Curatolo, *et al.*, "Energy-efficient low-Fresnel-number Bessel beams and their application in optical coherence tomography," Opt. Lett. **39**, 548–551 (2014).
27. H. Pahlevaninezhad, M. Khorasaninejad, Y.-W. Huang, *et al.*, "Nano-optic endoscope for high-resolution optical coherence tomography *in vivo*," Nat. Photonics **12**, 540–547 (2018).

28. M. N. Romodina and K. Singh, “Depth of focus extension in optical coherence tomography using ultrahigh chromatic dispersion of zinc selenide,” J. Biophotonics **15**, e202200051 (2022).
29. A. R. Tumlinson, B. Považay, L. P. Hariri, *et al.*, “*In vivo* ultrahigh-resolution optical coherence tomography of mouse colon with an achromatized endoscope,” J. Biomed. Opt. **11**, 064003 (2006).
30. D. Wang, B. V. Hunter, M. J. Cobb, *et al.*, “Super-achromatic rapid scanning microendoscope for ultrahigh-resolution OCT imaging,” IEEE J. Sel. Top. Quantum Electron. **13**, 1596–1601 (2007).
31. J. Xi, A. Zhang, Z. Liu, *et al.*, “Diffractive catheter for ultrahigh-resolution spectral-domain volumetric OCT imaging,” Opt. Lett. **39**, 2016–2019 (2014).
32. W. Yuan, R. Brown, W. Mitzner, *et al.*, “Super-achromatic monolithic microprobe for ultrahigh-resolution endoscopic optical coherence tomography at 800 nm,” Nat. Commun. **8**, 1531 (2017).
33. Z. Yaqoob, J. Wu, and C. Yang, “Spectral domain optical coherence tomography: a better OCT imaging strategy,” BioTechniques **39**, S6–S13 (2005).
34. D. J. Harper and B. J. Vakoc, “Relationship between axial resolution and signal-to-noise ratio in optical coherence tomography,” Opt. Lett. **47**, 1517–1520 (2022).
35. M. Muller, *Introduction to Confocal Fluorescence Microscopy* (SPIE Press, 2006).
36. https://github.com/lseon945/Chromatic-OCT.